This article was downloaded by: [Tiantian Feng]
On: 18 February 2014, At: 18:35
Publisher: Taylor & Francis
Informa Ltd Registered in England and Wales Registered Number: 1072954 Registered office: Mortimer House, 37-41 Mortimer Street, London W1T 3JH, UK

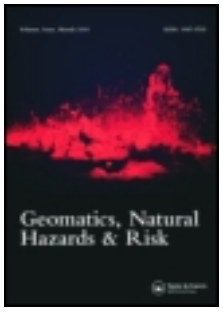

Geomatics, Natural Hazards and Risk
Publication details, including instructions for authors and subscription information:
http://www.tandfonline.com/loi/tgnh20

Some applications of 2-D and 3-D photogrammetry during laboratory experiments for hydrogeological risk assessment

M. Scaioni[a], T. Feng[a], L. Barazzetti[b], M. Previtali[b], P. Lu[a], G. Qiao[a], H. Wu[a], W. Chen[a], X. Tong[a], W. Wang[a] & Ron Li[ac]

[a] Center for Spatial Information Science and Sustainable Development Applications, Tongji University, Shanghai, P.R. China

[b] Department of Architecture, Built Environment and Construction Engineering (ABC), Politecnico di Milano, Italy

[c] Mapping and GIS Lab, Ohio State University, Columbus, Ohio, USA

Published online: 13 Feb 2014.

To cite this article: M. Scaioni, T. Feng, L. Barazzetti, M. Previtali, P. Lu, G. Qiao, H. Wu, W. Chen, X. Tong, W. Wang & Ron Li , Geomatics, Natural Hazards and Risk (2014): Some applications of 2-D and 3-D photogrammetry during laboratory experiments for hydrogeological risk assessment, Geomatics, Natural Hazards and Risk, DOI: 10.1080/19475705.2014.885090

To link to this article: http://dx.doi.org/10.1080/19475705.2014.885090

PLEASE SCROLL DOWN FOR ARTICLE

Taylor & Francis makes every effort to ensure the accuracy of all the information (the "Content") contained in the publications on our platform. However, Taylor & Francis, our agents, and our licensors make no representations or warranties whatsoever as to the accuracy, completeness, or suitability for any purpose of the Content. Any opinions and views expressed in this publication are the opinions and views of the authors, and are not the views of or endorsed by Taylor & Francis. The accuracy of the Content should not be relied upon and should be independently verified with primary sources of information. Taylor and Francis shall not be liable for any losses, actions, claims, proceedings, demands, costs, expenses, damages, and other liabilities whatsoever or howsoever caused arising directly or indirectly in connection with, in relation to or arising out of the use of the Content.

This article may be used for research, teaching, and private study purposes. Any substantial or systematic reproduction, redistribution, reselling, loan, sub-licensing,

systematic supply, or distribution in any form to anyone is expressly forbidden. Terms & Conditions of access and use can be found at http://www.tandfonline.com/page/terms-and-conditions

Downloaded by [Tiantian Feng] at 18:35 18 February 2014

Geomatics, Natural Hazards and Risk, 2014
http://dx.doi.org/10.1080/19475705.2014.885090

Taylor & Francis
Taylor & Francis Group

Some applications of 2-D and 3-D photogrammetry during laboratory experiments for hydrogeological risk assessment

M. SCAIONI†, T. FENG†*, L. BARAZZETTI‡, M. PREVITALI‡, P. LU†, G. QIAO†, H. WU†, W. CHEN†, X. TONG†, W. WANG† and RON LI†§

†Center for Spatial Information Science and Sustainable Development Applications, Tongji University, Shanghai, P.R. China

‡Department of Architecture, Built Environment and Construction Engineering (ABC), Politecnico di Milano, Italy

§Mapping and GIS Lab, Ohio State University, Columbus, Ohio, USA

(*Received 15 August 2013; accepted 15 January 2014*)

Scaled-down flume tests are largely used to support investigations for the assessment of hydrogeological risk. Achieved outcomes can be integrated to numerical analyses for the study of unstable slope collapse, debris transport, and hydrological models in general. In the set-up of such simulation platforms, a relevant role has to be given to the Spatial Sensor Network (SSN) which is in charge of collecting geo-referenced, quantitative information during experiments. Photogrammetry (including 3-D imaging sensors) can play an important role in SSN because of its capability of collecting information covering wide surfaces without any contact. The aim of this paper is to give an overview and some examples of the potential of photogrammetry in hydrogeological simulation experiments. After a general introduction on a few preliminary issues (sensors, calibration, ground reference, usage of imaging or ranging sensors), potential applications are classified into 2-D and 3-D categories. Examples are focused on a scaled-down landslide simulation platform, which has been developed at Tongji University (Shanghai, P.R. China).

Downloaded by [Tiantian Feng] at 18:35 18 February 2014

1. Introduction

1.1. Measurements in hydrogeological simulations

The construction of scaled-down flume models has been largely exploited to support investigations for the assessment of hydrogeological risk. Achieved outcomes can be integrated and assimilated to numerical analyses for the study of unstable slope collapses (Feng et al. 2012), debris transport processes (Pozzoli et al. 2004), hydraulic models (Chandler et al. 2003; Kabdasli et al. 2004), rainfall- or earthquake-induced landslides (Fukuzono 1990), soil erosion (Rieke-Zapp & Nearing 2005; Gessese et al. 2010; Heng et al. 2010), and drainage basin evolution (Brasington & Smart 2003). Also application for experiments in the field of ecohydrology can be found (Rossi & Ares 2012). Some examples of simulation platforms are reported in figure 1.

Some *triggering factors* are introduced in each simulation platform to reproduce natural or anthropogenic causative reasons. For example, the load of a foundation

*Corresponding author. Email: fengtiantian@tongji.edu.cn

© 2014 Taylor & Francis

Figure 1. Some examples of flume models established for modelling different hydrogeological processes. Starting from the upper-left subfigure and going in clockwise direction: (*a*) the landslide simulation platform established at Tongji University (Shanghai, P.R. China); two different kinds of flumes for the analysis of shallow landslides at (*b*) the University of Parma, Italy (Roncella et al. 2004) and (*c*) Chengdu University of Technology, P.R. China (credit given to Runqiu Huang); (*d*) a reconstructed hydraulic model for studying debris flow accumulation in mountain environment (Politecnico di Milano, Italy; Pozzoli et al. 2004).

Downloaded by [Tiantian Feng] at 18:35 18 February 2014

over ground can be artificially obtained by using a vertical loading machine. The progressive load can be directly measured along the experiment. In the case of rainfall-induced landslides, water is distributed over a scaled-down model of slope or inside the soil to simulate underground water flow. In the case of loading, the triggering source is direct, while in the case of artificial rainfall it is indirect. The triggering factors usually result in some *final effects*, e.g. the collapse of a slope or a specimen, or the accumulation of debris and alluvium along a scaled-down riverbed. Some quantities can be directly observed to be related to the final effects, like displacements or volume of accumulated material. In many cases, also some *intermediate processes* can be observed, establishing an indirect link between triggering factors and final effects. An example of such quantities is the pore water pressure inside the landslide body that can be measured during a flume experiment.

In the set-up of a simulation platform, a relevant role has to be given to the *spatial sensor network* (SSN) which is in charge of collecting geo-referenced, quantitative information during experiments. The completeness of observations allows one to maximize the amount of information data achievable from a single or a set of tests. The availability of the sensor positions can be exploited for the analysis of spatial correlations between observations at different locations. Results can be *assimilated* to numerical models to better estimate the model's parameters (Gigli et al. 2011). An SSN also comprehends the information communication infrastructure, and devices for visualization, data storage, and analysis (see, e.g., Scaioni et al. 2013).

Limiting here the discussion on the sensor network, the adopted technology can be classified into *contact*, *remote*, and *environmental* sensors. The first group collects those that can record *geometric* (spatial position, relative displacements, local deformations, rotations), *geotechnical*, and *hydraulic* parameters. *Environmental* sensors are used for recording meteorological data. The third group is based on non-contact *remote* sensors whose aim is chiefly to give an overview of the processes over a large surface of the experiment body either from a qualitative (e.g., a video of the experiment run) or a quantitative side. In the second case, geometric information can be obtained thanks to photogrammetry and 3-D imaging techniques, but also other properties like surface temperature can be gathered by using proper sensors such as infrared thermal cameras (Budzier & Garlach 2011). Modern *digital photogrammetry* (Luhmann et al. 2013), including 3-D scanning and 3-D imaging sensors, is today a well-assessed technique for modelling the static 3-D shape of objects. On the other hand, it can be also applied for monitoring purpose, i.e., for measuring changes on the surface of a specimen/model along time. Thanks to this capability, photogrammetry may play an important role in the remote sensor group of the SSN (see Section 1.2). Indeed, it can provide information related to 2-D and 3-D modifications of surfaces with high-frequency, accuracy, and spatial resolution. The aim of the paper is not to give an exhaustive overview of the potential photogrammetric applications, but to suggest some useful methods that could be of large interest in the field of hydrogeological laboratory simulations.

While contact and environmental sensors usually collect *real-time* information and can be used for prediction purpose in real- or quasi-real-time (i.e., with a short delay), remote sensors are chiefly adopted at the *post-processing* stage.

The paper is expected to give to researchers some tools to develop their own laboratory experiment set-ups. In fact, one characteristic of such kind of test is the wide scenario of situations to be modelled, then the necessity of tailoring the SSN to each specific case. Consequently, the users should preferably know some principles of main photogrammetric key methods to be implemented and modified case-by-case rather than having a set of off-the-shelf techniques whose practical utility would be quite small.

1.2. Photogrammetry for laboratory experiments

Photogrammetric techniques have been widely exploited for measurements in laboratory experiments on construction materials (see, e.g. Maas & Hampel 2006; Barazzetti & Scaioni 2009, 2010; Roncella et al. 2012). In particular, the diffusion of digital cameras and the increase of automation in modern digital photogrammetry fostered its application to this field with respect to the era of film cameras. In fact, the most important improvement related to the use of digital images does not consist of the greater achievable precision (see Fraser 1992, for example) but in the simplification and economical sustainability of its application. No special and expensive cameras are still needed, but a quite standard consumer digital camera can be used after proper *calibration*, i.e., the process for reconstructing the intrinsic camera geometry and modelling lens distortion (Luhmann et al. 2013). Furthermore, all processing stages can be done using regular computers, without requiring optical-mechanics apparatus like in the past. Automation of both orientation and calibration stages has simplified and reduced the work the operator has to carry out (Fraser 2013). The

Downloaded by [Tiantian Feng] at 18:35 18 February 2014

stereoscopic plotting, the only way to derive three-dimensional surfaces from photos, has been replaced by automatic digital surface reconstruction, which works well in many applications (Grün 2012).

The diffusion of digital techniques and the availability of low-cost photogrammetric software packages allowed a larger number of people to accomplish image-based 3-D reconstruction projects where high precision is required (Chandler et al. 2005). On the other hand, the quality of results still depends on the experience and background of the users.

Photogrammetry shows typical advantages of non-contact techniques, offering the chance to evaluate displacements or changes over larger areas than on single points like contact sensors can do. Moreover, in the case fast processes (like debris flow run-outs) have to be investigated images can be acquired using high-speed cameras (Roncella et al. 2004; Watanabe et al. 2005; Tiwari et al. 2007).

Not only does modern photogrammetry account for standard 2-D cameras, but it may take advantage of the so called *active 3-D imaging sensors* (Remondino & Stoppa 2013). These can directly collect 3-D data, unlike photogrammetry which needs to intersect rays from two known camera stations for extracting 3-D information.

In experiments for testing hydrogeological models, usually a process is simulated at a small scale. First of all, photogrammetry and 3-D imaging sensors can be adopted for the precise reconstruction of the real geometry of the testing environment. This process requires gathering a block of images (or 3-D views in the case of active 3-D imaging sensors) from different positions, so that the whole surface can be modelled. This application is a quite standard process and readers can find exhaustive information in the literature (e.g., Luhmann et al. 2013). More interesting from the scientific point of view is the use of photogrammetric techniques for dynamic observation of the external surfaces of the specimen during a simulation experiment. Such measurements might include (i) the changes of shape (deformations, transportation, and deposit of material), (ii) point or feature displacements and tracking, and (iii) crack analysis (detection and measurement).

In order to demonstrate the technical feasibility of the methods proposed in the paper, some implementations carried out at Tongji University (Shanghai, P.R. China), in cooperation with Politecnico di Milano university (Italy), are presented and discussed. For this reason, some basic information on the simulation platform established at Tongji University is given in Section 1.3.

In Section 2 some background on key aspects related to the application of photogrammetry are discussed. Then, applications are classified into two main categories, depending if the surveyed object can be approximated in 2-D or 3-D space (Sections 3 and 4, respectively). This option will involve a different geometric model for relating the 2-D image space of one or more images to the three-dimensional object space. Finally some conclusions are drawn in Section 5.

1.3. The landslide simulation platform at Tongji University, Shanghai

A scaled-down platform for the simulation of rainfall-induced landslides was established in the campus of Tongji University, Shanghai. The main purpose of this facility was to test the SSN to be used in a real-scene environment. The model (see the upper-left image in figure 1) was designed to reproduce some characteristics such as inclination, soil layers, and composition of a ground slope in Taziping (Sichuan

Downloaded by [Tiantian Feng] at 18:35 18 February 2014

province, P.R. China). On this site, an active landslide was triggered after the Wenchuan earthquake on 12 May 2008. To emulate the real slope, the model was divided into three sectors with inclinations of 5°, 15°, and 30°, respectively. Two soil layers of different materials were laid down.

The sensors used in the simulation platform are representative of the more extensive equipment to be adopted for monitoring real landslides. The group of *contact sensors* installed included some geotechnical sensors (a set of piezometers, one osmometer and other sensors for measuring underground water pressures), inclinometers, extensometers, and accelerometers. The *remote sensors* consisted of cameras able to capture images at different speeds and resolutions. A pair of synchronized high-speed monochromatic cameras DALSA Falcon 4M60, a pair of low-speed single-lens reflex (SLR) colour cameras Nikon D200, and one infrared video-camera for surveillance purpose, were adopted. Properties of these cameras are reported in table 1. Eventually, a weather station and a rain gauge were integrated into the SSN to record meteorological parameters and to perform weather forecast.

All sensors installed on the simulation platform were connected to a control unit which synchronized data acquisition and dealt with data broadcasting to a server station located in the monitoring control room about 800 m away. The server hosted a database that had been designed and implemented to store all recorded signals. Data retrieving could be performed in real time for visualization purpose in a special control room.

More details on different aspects of this project can be found in Feng et al. (2012), Qiao et al. (2013), and Scaioni et al. (2013).

Downloaded by [Tiantian Feng] at 18:35 18 February 2014

2. Technical background

2.1. *Sensors adopted in digital photogrammetry*

2.1.1. Digital cameras. Digital cameras are the main sensors adopted in photogrammetry. While in the past only special 'metric' or 'semi-metric' cameras were used (Kraus 2008), modern digital photogrammetry can be afforded with standard consumer cameras after *calibration*. Photogrammetry is based on measuring point coordinates on the images and the successive intersection of corresponding rays in space. This task requires establishing a reference system that in digital images can be defined on the basis of the regular pixel grid. A procedure called *camera calibration* allows the user to determine the basic parameters (the *principal distance c* and the

Table 1. Technical features of cameras adopted in the landslide simulation platform at Tongji University (SLR: single-lens reflex; IND: industrial; MC: mirrorless compact).

Camera	Type of camera	Sensor	Sensor size adopted	Pixel size	Focal length	Max. data acquisition rate
Nikon D200	SLR	CCD	2,896 × 1,944 pix[(1)] 23.6 × 15.8 mm	8.1 μm	35 mm	5 Hz
DALSA Falcon 4M60	IND	CMOS	2,352 × 1,728 pix 17.4 × 12.8 mm	7.4 μm	24 mm	62 Hz
Nikon V1	MC	CMOS	3,872 × 2,592 pix 13.2 × 8.8 mm	3.4 μm	10 mm	60 Hz

[(1)]In the application described here the maximum resolution of this camera (3,872 × 2,592 pix) was not exploited, as described in Section 4.2.

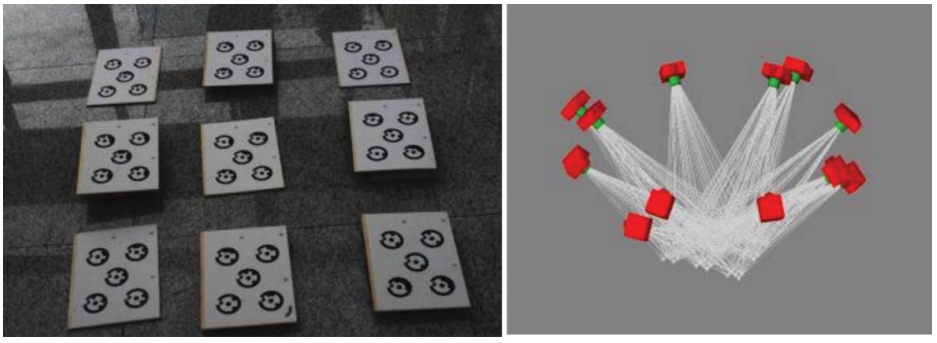

Figure 2. Examples of coded targets to be adopted for camera calibration and their spatial layout (left). Typical geometry of a block of convergent images used for camera calibration (right).

Downloaded by [Tiantian Feng] at 18:35 18 February 2014

principal point coordinates x_0, y_0) that are required for modelling the inner formation process of an image, addressed to as *inner orientation* (IO). In addition, some *additional parameters* (AP) to compensate for lens distortion are estimated. The reader may refer to Luhmann et al. (2013) and Fraser (2013) for more details.

As a rule of thumb, calibration is always suggested yet it could be avoided in 2-D applications when a low precision is needed (at level of pixel size). Indeed, nowadays this task can be accomplished in an easy way, due to the availability of several low-cost (or also free) software packages allowing the rigorous photogrammetric calibration of any camera. The user has to capture a set of images (4–15) with the same camera from different positions, all depicting a set of coded targets[†] (see an example in figure 2). The resulting images are processed in a fully automatic way to derive the calibration parameters to be used for the next photogrammetric application of the camera. Focusing distance and focal length changes in zoom lenses both affect calibration parameters. Consequently, they must be kept at the same set-up during both calibration and application stages.

Standard single-lens reflex (SLR) or mirrorless compact (MC) cameras can acquire RGB (red-green-blue) images, while some industrial (IND) cameras for metrological applications can gather monochromatic intensity images only. Basically, photogrammetry does not require colour images, except in the cases where it is done for documentation or 3-D visualization purpose (for example in the field of cultural heritage). On the other hand, different colour components follow a slightly different path inside the lens due to different wavelengths. This results in the generation of misaligned images corresponding to the basic RGB colours. While this problem does not have any practical influence on most applications, when a subpixel precision is required, the user is suggested to work with the green channel only.

Indeed, in CCD and CMOS sensors that are commonly adopted in RGB digital cameras, the elementary photodiodes do not capture all colours along with the same geometric scheme (called 'Bayer' scheme). The colour which is captured in the more symmetric way is just green.

[†]The use of targets is not strictly needed. Indeed, camera calibration can be performed in a markerless fashion as proposed in Barazzetti (2011). However, the use of targets allows anybody to accomplish this procedure in a precise and reliable way.

The selection of the camera depends basically on the required precision of the reconstruction. The focal length controls the average scale between the real object and its image recorded by the sensor. Consequently, it largely affects the precision of photogrammetric measurements. As a rule of thumb, a rough estimation of precision obtainable from single or stereo-camera systems can be derived from using simplified formulas of the so-called 'normal case of stereo-photogrammetry,' whose reference can be found in any handbook (e.g., in Kraus 2008; Luhmann et al. 2013). Basically a pair of cameras with the sensors approximately in parallel and aligned positions is considered. The average precision (in term of standard deviation $\sigma_{X,Y}$) of the achievable measurements in one of the directions X and Y parallel to sensors can be worked out as follows:

$$\sigma_{X,Y} = \frac{Z}{f}\sigma_{\text{imm}}. \tag{1}$$

where Z is the distance from the camera of the considered point in the object space and σ_{imm} is the precision of each image coordinate measurement, depending on the method used for collimation (manual or automatic), and on the type of measured point (distinct or smooth natural feature, target), and f is the focal length. Equation (1) may also be used for a rough evaluation of precision in case a simplified reconstruction model based on a single image is adopted (see Section 3).

The precision σ_Z along the direction Z, i.e. along depth, also depends on the distance B (*baseline*) between the two camera stations:

$$\sigma_Z = \frac{Z^2}{Bf}\sqrt{2}\sigma_{\text{imm}}. \tag{2}$$

In practice, several times stereo-cameras are slightly rotated to have a convergent configuration that results in precision improvement along the Z direction (Fraser 1996). Equations (1) and (2) may give a reasonable approximation of the achievable precision also in the case of slightly convergent images.

Two other important geometric parameters for the selection of the camera are the size of the sensor $W \times H$ (width and height) and the number of pixels $n_r \times n_c$ along row and column directions. The former pair of parameters contributes to defining the portion of the object that can be depicted in a single image, together with the focal length f. The latter pair influences the resolution and the precision of measurements, because the size of each pixel is $p = W/n_c = H/n_r$ (usually p *is* the same for rows and columns). The precision of image measurement is roughly given as $\sigma_{\text{imm}} = kp$, being the value of k depending on the method adopted for image measurement. For example, a value $k = 1$ can be used if points are measured manually, while lower values are applied when measurement is accomplished by automatic *image matching* techniques (Grün 2012): $k = 0.3{-}0.5$ if a *feature-based matching* (FBM) method is applied, $k = 0.1{-}0.3$ for *area-based matching* (ABM), and $k = 0.05{-}0.1$ in the case of signalized targets. After these considerations, it might seem obvious that a larger number of pixels are an advantage, because they would lead to improvement of precision and resolution. On the other hand, the larger the number of pixels, the more will be the noise in the image, especially with small-size CMOS sensors.

Downloaded by [Tiantian Feng] at 18:35 18 February 2014

The last aspect to consider is the required image acquisition rate, which depends on the dynamic of the process under observation. In several cases, the same experiment may entail different phases where the surface changes at various velocities. Generally, displacements may be very slow at the beginning, with a sudden acceleration in proximity of the final collapse. Generally SLR and MC cameras are suitable up to a frequency of 0.5–1 Hz, while industrial cameras should be used when higher frequencies are needed. Some up-to-date consumer-grade cameras, like the Nikon V1 reported in table 1, allow the acquisition of high-frequency images, but along a short time span and a smaller resolution than the real sensor size. This limits their applications for recording high-frequency videos during experiments. The latter sensors cannot be used in an autonomous way, but have to be connected to the data acquisition software that is used for their set-up and for real-time downloading. Such packages can also deal with the synchronization of more sensors to be used together, a task that is really critical when the reconstruction of fast processes is needed. Today several engineered solutions are provided by the vendors, but also it's quite easy to build up tailored data acquisition tools by using assisted environments like Matlab® or LabView®.

Downloaded by [Tiantian Feng] at 18:35 18 February 2014

2.1.2. Active 3-D imaging sensors. An alternative approach to image-based photogrammetry relies on *active 3-D imaging sensors*. These can directly collect three-dimensional surfaces without any further processing stage, except that for registration of multiple 3-D views and for the final information extraction. Each sensor may have its own calibration model and methods for its accomplishment.

Long-range laser scanners are widely used for topographic modelling of real slopes (Pirotti et al. 2013a), including the chance of filtering vegetation thanks to full-waveform sensors (Pirotti et al. 2013b). In a similar way, active 3-D imaging sensors are ideal for reconstructing surfaces in case the area is limited to a few square metres and less. Their use is discouraged in favour of industrial high-speed cameras when a higher acquisition rate is needed, and when the aim is to extract features or to track points. This category entails many different kinds of sensors featuring non-standardized properties (like digital cameras basically do). Broadly speaking active 3-D imaging sensors that can be used for close-range applications can be categorized into the following classes (see more details in Guidi et al. 2010):

(1) Triangulation scanners based on points, lines, patterns;
(2) Time-of-flight (ToF) and triangulation cameras;
(3) Phase-shift laser scanners.

Generally, category (1) comprehends sensors that outperform the requirements of hydrogeological experiments. A point precision up to 0.1 mm and a point density of 1 mm grid can be reached with ease. Sensors that go beyond these limits also are available but their field of view (FoV) is usually limited to a few tens of square decimetres. In the case bigger static scenes should be reconstructed with higher precision and there is no limitation on surveying time, *hand-held triangulation scanners* can be used. However, usually they require putting some targets on the object surface. If lower precision (at 1–2 cm level) and higher acquisition rate (more than 10 Hz) are required, an interesting option is given by *ToF* and *triangulation cameras*, including those in the *gaming device* class (e.g., the Microsoft Kinect®). The advantage of using

such devices is their low cost (about one hundred euros for gaming devices and up to one thousand for other systems), although they require the user to carry out sensor calibration on his own for performance improvement (Remondino & Stoppa 2013). The last class of sensors (3) can be used to cover larger area and give precision in the order of a few millimetres. On the other hand, their speed is lower because the acquisition is done point-by-point and not on full matrices such as sensors in category (2). On the other hand, *phase-shift laser scanners* may support hydrogeological experiments when larger infrastructures are needed (see for example the flume in figure 1 (*c*)). As the limited data acquisition speeds the bottleneck of their application, the following formula can be adopted to work out the time T_{scan} needed to cover a scene whose area is A:

$$T_{\text{scan}} = \frac{A}{\theta^2 \overline{d}^2} \cdot \frac{1}{f_{\text{scan}}}, \tag{3}$$

where θ is the angular scanning resolution (in radians), which is supposed to be the same along both horizontal and vertical directions; $\overline{d}$ is the average distance from the scanner; and f_{scan} is the scanning frequency. If the process under investigation is faster than computed T_{scan}, this means that the instrument under assessment is not suitable.

2.2. *Datum definition*

In standard close-range photogrammetry some *ground control points* (GCP), whose coordinates have been measured independently (e.g., by using a theodolite), are usually placed on the surface of the object to reconstruct or close to it. The aim of GCPs is twofold: (1) to establish the *datum* to compute point coordinates, i.e., the *ground reference system* (GRS); and (2) to enforce the block geometry in the case many images are needed, or the spatial distribution is weak; this happens if the block has an elongated shape, if the overlap between some close images is low, or if they feature large convergent angles among them. While problem (1) refers to both 2-D and 3-D applications, the second only concerns the three-dimensional case. Indeed, in 2-D applications usually a single camera station is employed.

Generally the use of GCPs makes photogrammetry more complicated, because it requires a second measurement instrument and the deployment of targets on the object. Targets are points that can be identified and measured with ease in both the images and on the real object. One of the advantages of modern digital photogrammetric techniques is that the use of GCPs can be avoided in many situations. First of all, a redundant number of digital images can be collected with ease to improve the computation of the *exterior orientation* (EO). This consists of the position and attitude of each camera station with respect to a given GRS. Second, EO can be reckoned on the basis of *tie points*. These are corresponding points that are measured on more images by manual or automatic procedures, with or without targets. The main advantage of tie points is that they do not need to be measured in the GRS. Thanks to a computational procedure called *free-net bundle adjustment* (Luhmann et al. 2013) all images can be oriented into an 'arbitrary' GRS, whose position with respect to the object is defined up to an unknown 3-D *similarity* transformation. In many applications the definition of all seven parameters (three shifts, three rotations in

Downloaded by [Tiantian Feng] at 18:35 18 February 2014

space, and one isotropic scale) of the similarity transformation is not necessary. For instance, if the reconstructed geometry of the object is adopted only to do relative measurements, the knowledge of the real distance between two points may suffice to fix the global scale factor. Moreover, the 'arbitrary' GRS can be also rotated by using a vertical element in the scene to define the z axis, and a horizontal feature to align the direction of x or y axes.

In the case where other three-dimensional data such as those from an active 3-D imaging instrument should be referred into the same GRS, some tie points can be defined in the photogrammetric reconstruction for registration purpose. These points have to be visible in both data-sets.

In the case a 3-D scanning or a 3-D imaging sensor is adopted, one static station may suffice if the entire scene can be covered into the instrument FoV. Consequently, the intrinsic reference system of the adopted instrument can be used to define the GRS. Also in this case, the knowledge of some horizontal or vertical features may help shift and rotate the whole three-dimensional model, while the scale is fixed owing to the direct measurement of range performed by such sensors. In the case of large blocks, including several scans for the survey of static scenes, problems similar to those encountered with image-based photogrammetry have to be considered (Vosselman & Maas 2010).

In 2-D applications it is also possible to get rid of GCPs for computing the geometric transformation that maps point coordinates from image-to-ground space, as demonstrated in Section 3.

Downloaded by [Tiantian Feng] at 18:35 18 February 2014

3. 2-D applications

3.1. Theoretical aspects

When the surface to reconstruct is approximately flat, the transformation between *image* and *object* coordinates is given by a 2-D *homography*. This means that a photogrammetric system made up of a single camera station imaging the whole area of interest will suffice for the reconstruction purpose. The *homography* transformation is described by a 3×3 non-singular matrix $\mathbf{H}$:

$$\mathrm{x} = \begin{bmatrix} x \\ y \\ 1 \end{bmatrix} = \begin{bmatrix} h_1 & h_2 & h_3 \\ h_4 & h_5 & h_6 \\ h_7 & h_8 & h_9 \end{bmatrix} \begin{bmatrix} X \\ Y \\ 1 \end{bmatrix} = \mathbf{H}\mathbf{X} \tag{4}$$

where vectors $\mathrm{x} = [x\ y\ 1]^{\mathrm{T}}$ and $\mathrm{X} = [X\ Y\ 1]^{\mathrm{T}}$ express image and object coordinates of a generic point in homogenous coordinates, respectively. In this case, the GRS has only two degree-of-freedom (DoF), being the object planar. If the object is only approximately flat, the assumption of model in equation (4) will lead to errors in the computed coordinate vector X. These errors can be evaluated with a simple formula that works out the radial error (δr) in the object plane as function of the off-plane distance (ΔZ) of a point:

$$\delta r = \frac{\Delta Z \cdot r}{Z}, \tag{5}$$

where Z is the distance from the camera to the average object plane and r is the distance of the considered point from the principal point.

The estimate of matrix **H** requires the determination of eight parameters since its scale can be arbitrarily fixed. A common method to overcome the problem is based on a set of non-aligned GCPs (at least four) whose coordinates are known in the 2-D GRS and can be also measured in the image. Moreover, equation (4) shows that: (i) one image is enough for reconstructing planar objects and (ii) the inverse transformation can be always worked out because **H** matrix is non-singular.

On the other hand, GCPs are not always available. Some other methods exploit the presence of some orthogonal lines, which can be identified in one image. In the solution proposed in Barazzetti (2011), the homography parameters can be computed on the basis of two sets of parallel lines in the image plane (not necessarily parallel between them as in the most popular methods), coupled with the knowledge of the *calibration matrix*:

$$\mathbf{K} = \begin{bmatrix} c & 0 & x_0 \\ 0 & c & y_0 \\ 0 & 0 & 1 \end{bmatrix}. \tag{6}$$

The IO parameters in equation (6) can be recovered from camera calibration, as described in Section 2.1.1. Image distortion is not accounted for in matrix (6) and image point coordinates should be corrected beforehand, or distortion-free images should be generated. Information in calibration matrix **K** is sufficient to recover metric properties without acquiring metric data in the object plane (e.g., known ratios of distances and angles, object points). There will be only an overall scale ambiguity that should be removed by measuring a real distance with a graduated tape. The *vanishing line* (Hartley & Zissermann 2006) is computed from a couple of lines which define a parallelogram in the image (see figure 3). Given a couple of parallel lines l

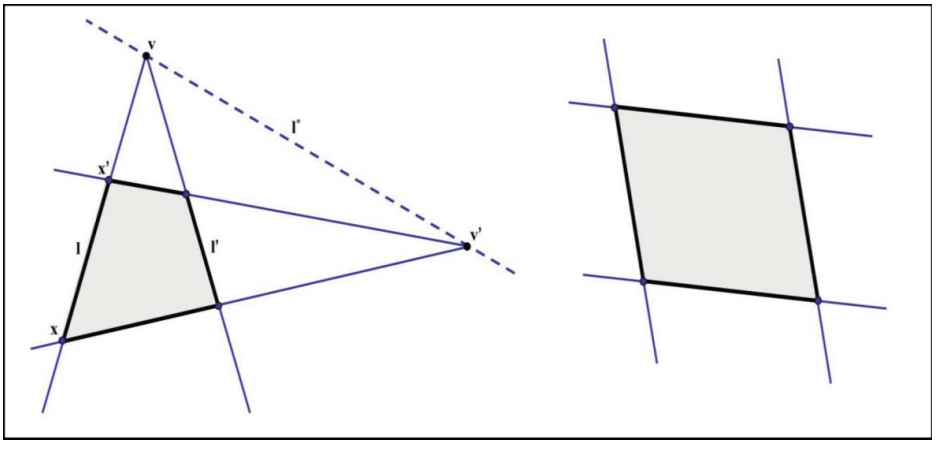

Figure 3. Geometric quantities used for image rectification according to Barazzetti (2011). On the left, a generic parallelogram in the image plane, that is usually distorted because of perspective deformations (the dotted blue line is the *vanishing line*). On the right, the undistorted parallelogram.

Downloaded by [Tiantian Feng] at 18:35 18 February 2014

and l′, their intersection gives their *vanishing point* $v^* = l \times l'$ ('×' is the vector product). The identification of the *vanishing line* can be carried out by using two vanishing points: $l^* = v^* \times v^{*\prime}$. In the case of multiple parallel lines, the intersection problem is solved via Least Squares (LS). The estimation of the rectifying transformation is performed through homography:

$$\mathbf{H} = \mathbf{KUK}^{-1}, \tag{7}$$

where matrix $\mathbf{U} = [u_r\ u_s\ u_n]$ is made up of a set of vectors that form an orthonormal set. The unary vector u_n is derived from the normal vector n to the plane as $u_n = n/\|n\|$, where $n = \mathbf{K}^{\mathbf{T}} l^*$. This leads to another ambiguity (a rotation around the normal vector n in this case), because there is an infinite number of vectors perpendicular to *n*. The triad of orthonormal vectors u_r, u_s, and u_n must be estimated with some constraints applied to the second vector u_r in order to take into consideration possible degenerate configurations. The last vector can be estimated with a simple vector product. The homography matrix H is estimated through equation (4) that allows transforming the image into a 2-D metric space, but with ambiguity in the overall scale.

3.2. Example

The image rectification method described in Section 3.1 was applied to a set of 5 images captured during a landslide simulation experiment (see Section 1.3). Images were captured with a hand-held digital camera Nikon V1 (see table 1 for technical properties) that had been previously calibrated. Image distortion was removed from all images beforehand. As can be seen in the example reported in figure 4, these images depict one of the lateral transparent windows of the simulation platform. Through this window the lateral ground profile during landslide development can be recorded. Therefore images have to be rectified and registered in the same reference system for comparison.

The procedure for image rectification was based on the extraction of the parallel lines that form the frame around the window. These were then used to compute the vanishing line needed to build up the matrix **U** in equation (7). The initial homography $\mathbf{H}_0$ was computed by using the calibration matrix **K** containing the IO parameters derived from camera calibration. One image of the sequence (the one in figure 4

Figure 4. One of the images of the sequence (the one used as master) before (left) and after rectification (right).

Downloaded by [Tiantian Feng] at 18:35 18 February 2014

at left) was rectified at the beginning of the process and became the reference ('master') for the co-registration procedure of all the remaining images.

To automate the registration of the following images, all of them were matched with respect to the 'master' image by using the SIFT operator (Löwe 2004) for extracting a dense set of tie points. SIFT operator is a feature detection algorithm invariant to image shift, rotation, scale, and brightness transformations. It also maintains a certain degree of stability under perspective and affine transformations. This algorithm is usually used to find corresponding points between different images for registration purpose. Indeed, in close-range photogrammetry the invariance properties of SIFT have been largely exploited, because images in a block can feature relevant differences regarding the geometric and radiometric content. SIFT allows not only the automatic orientation of 3-D close-range blocks (see e.g. Barazzetti & Scaioni 2010), but also the registration of multi-temporal image sequences.

A set of points was extracted from the first rectified image and was used as GCPs for the rectification of the remainders. In this second case, these GCPs allowed to compute the homography matrix Hi of each *i*th image of the sequence by using a standard point-to-point method. The method provided the whole sequence of 20 images captured during an experiment, from which it was possible to draw the ground profile at different times. Images were stored as standard GEOTIFF files in order to overlap them in a standard desktop GIS package. The first and last images of the rectified sequence and the profile extracted are shown in figure 5.

Because in this experiment only a small data-set of five images was used, the extraction of parallel lines to compute the vanishing points v^* and $v^{*\prime}$ as well as drawings the profiles in figure 5 were both accomplished manually. In the future, the implementation of these tasks in an automatic (or semi-automatic) way will simplify the application of this method to longer image sequences.

The overall precision achievable for the surface profiles depends on the three main stages of the procedure. In the first stage, one image is rectified to be used as geometric reference for the others. This task does not significantly influence the final precision of each profile, which basically depends on registration of the *i*th image with respect to the 'master' and the line extraction method. Registration is based on corresponding control points extracted with SIFT (precision about 0.6÷0.8 pixels). These points are used for the LS estimation of any homography matrix $\mathbf{H}_i$. The estimate of precision of each point in the rectified image *i*th can be approximately computed by

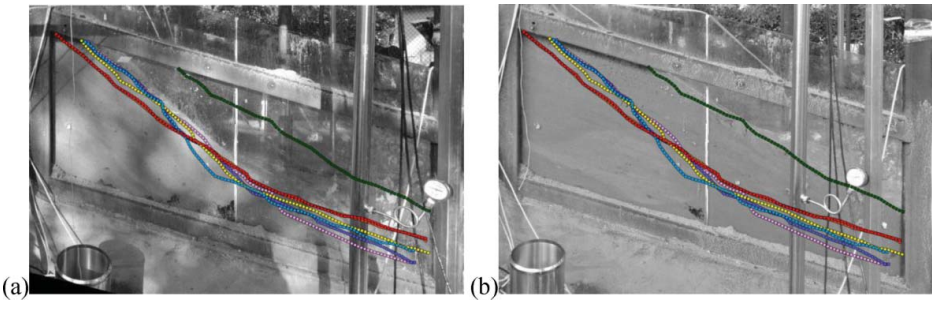

Figure 5. The first and last images of the sequence and some profiles extracted. It is evidently a progressive motion followed by a sudden collapse (green line).

Downloaded by [Tiantian Feng] at 18:35 18 February 2014

using variance–covariance propagation (index i has be omitted):

$$\mathbf{C}_X = \begin{bmatrix} \sigma_X^2 & \sigma_{XY} & 0 \\ \sigma_{XY} & \sigma_Y^2 & 0 \\ 0 & 0 & 0 \end{bmatrix} = \mathbf{H}^{-1}\mathbf{C}_x(\mathbf{H}^{-1})^{\mathrm{T}} = \mathbf{H}^{-1}\begin{bmatrix} \sigma_x^2 & 0 & 0 \\ 0 & \sigma_y^2 & 0 \\ 0 & 0 & 0 \end{bmatrix}(\mathbf{H}^{-1})^{\mathrm{T}}, \tag{8}$$

where $\mathbf{C}_\mathrm{X}$ and $\mathbf{C}_\mathrm{x}$ are the covariance matrices of point coordinates in the rectified and in the image reference system, respectively. Although in equation (8) some approximations on the stochastic model are introduced (parameters in homography matrix $\mathbf{H}$ are considered as constant values, and point coordinates x and y are uncorrelated), it may be helpful to evaluate point precision. Here an average precision of about $\sigma_\mathrm{X} = \sigma_\mathrm{Y} = 0.6$ pixels was found.

The extraction of profiles was instead carried out manually. As the line is well-defined and clearly visible in the images, the (human) operator was able to derive measurements with a precision of approx. $\sigma_{\mathrm{prof}} = 2.5$ pixels.

Overall the achieved precision of each point of the extracted profile can therefore be computed as:

$$\sigma_{X_\mathrm{prof}} = \sqrt{\sigma_X^2 + p\sigma_{\mathrm{prof}}^2}; \quad \sigma_{Y_{\mathrm{prof}}} = \sqrt{\sigma_Y^2 + p\sigma_{\mathrm{prof}}^2}, \tag{9}$$

where p is the average pixel size ($p = 1$ mm in this example). The precision of the extracted profiles in both directions is then $\sigma_{\mathrm{X_prof}} = \sigma_{\mathrm{Y_prof}} = 2.6$ mm) that can suffice for the analysis of this experiment.

4. 3-D applications

4.1. Theoretical aspects

If the object to survey cannot be approximated by a plane, the full perspective transformation from the object coordinates ($\mathrm{X} = [X\ Y\ Z]^{\mathrm{T}}$) of a generic point to its corresponding projection on the image ($\mathrm{x} = [x\ y\ -c]^{\mathrm{T}}$) is adopted. This is given by the *collinearity equations*:

$$\begin{bmatrix} x - x_0 - \Delta x \\ y - y_0 - \Delta y \\ -c \end{bmatrix} = \frac{1}{m}\mathbf{R}^{\mathrm{T}}(\mathrm{X} - \mathrm{X}_0), \tag{10}$$

where Δx and Δy express the correction for image distortion on the basis of the additional parameters (AP) computed during camera calibration; the *spatial rotation matrix* $\mathbf{R}$ and the *perspective centre vector* $\boldsymbol{X_0}$ define the EO of the image; the *scale factor* m is cancelled out by dividing the first two lines of equation (8) by the third one. In the case where distortion-free images have been generated, both corrective terms Δx and Δy can be ignored. Equation (10) can be used either for the computation of the unknown EO parameters, given some GCPs, or using a free-network bundle adjustment (see Section 2.2), and for the reconstruction of 3-D coordinates of points, given the EO. Usually the IO parameters (including AP for lens distortion correction) are computed at a preliminary stage, but it is also possible to compute them along the reconstruction project (*self-calibration*). A separation of these two

Downloaded by [Tiantian Feng] at 18:35 18 February 2014

procedures has to be generally preferred, in the opinion of the authors. Indeed, camera calibration and object reconstruction require two diverse block geometry. The requirements for calibration have been already discussed in Section 2.1.1 and are exemplified in figure 2. For the latter task, the block geometry strictly depends on the experiment set-up and is usually based on a small number of camera stations (2÷3), depending on the size of specimen/model.

Disregarding when calibration is computed, equation (10) is used for the computation of all calibration parameters as well, which can be included as additional unknowns.

The computation of EO is done through an LS *bundle adjustment*, where tie point and GCP (if used) image coordinates are used. Tie points can be manually measured by locating some natural features on the images, or by using *coded targets* (such as those used for camera calibration in figure 2), or by extracting *key points* in an automatic way with *image matching* algorithms (Grün 2012). The use of a rigorous LS procedure in the bundle adjustment gives the opportunity to locate errors (if not so many) in image points and to estimate the theoretical accuracy of computed 3-D points.

In lab experiments, very often only 2–3 fixed cameras are used for tracking point displacements and deformations over a small scene. The EO for such small configurations can be solved with ease without any GCP. In the case of multi-temporal data acquisition, EO can be computed before the experiment, and then used for all epochs if cameras are constrained to stable positions. In particular, when using the stereo-configuration made up of two cameras, there are different ways for describing the so-called *relative orientation* (RO), which can describe the pose of a camera with respect to the other. Some approaches are typical of photogrammetry and can be directly derived from the collinearity equations (Luhmann et al. 2013). Other methods have been developed in computer vision and are based on the use of projective transformations, with the advantage to be expressed in linear form (Hartley & Zissermann 2006). Different models have various parameterizations. Basically, a minimum number of five parameters are required to define the geometric relative position between the pair of images, but some methods involve more parameters. Anyway, these can be estimated on the basis of tie points without any knowledge about an external GRS. Once RO has been computed, points can be reconstructed in a three-dimensional space up to an ambiguous 3-D similarity transformation.

Downloaded by [Tiantian Feng] at 18:35 18 February 2014

4.2. Examples

While the spatial geometric relationship between points in image and object space can be established through the collinearity model (8) or from RO, a wide range of techniques can be applied for extracting information from the images after orientation. As already mentioned, photogrammetry can be used in a static way for the geometric modelling of a whole scene. In this case a block of images has to be gathered, where the camera is stationed in different positions. It is also possible to compare two 3-D reconstructions corresponding to different epochs during an experiment (e.g., before and after running). However, this approach requires some time to be accomplished and cannot be used for tracking dynamic scenes. Three-dimensional reconstruction of static scene is also an easy task with 3-D scanning systems, which in many cases is preferable with respect to the image-based methods because it

directly provides 3-D coordinates. In the case a dynamic scene has to be captured, the use of stable cameras in a stereo or multiple-view configuration is required.

In the following, an example of extracting three-dimensional information from images acquired during a landslide simulation experiment is reported. A high-resolution stereo-camera system was used here for data acquisition. The aim of this application is the computation of volume changes during an experiment carried out in the platform established at Tongji University.

A couple of SLR Nikon D200 cameras were placed in front of the flume in order to gather stereo-images during experiments. As can be seen in table 1, the maximum geometric resolution was not exploited here to improve the image quality (smaller images are less noisy) and to reduce the computational burden. Both cameras were kept in the same position during the whole experiment with a baseline of 1 m. A data acquisition rate of 2 frames per minute was set up. In figure 6 the camera set-up is shown. Before the experiment, both cameras had been independently calibrated. After the experiment, the first task was the computation of the RO of the stereo-camera system. This was accomplished by using some coded targets glued on the frame structure of the simulation platform to be used as tie points. The availability of 3-D coordinates of targets was exploited for transforming points obtained after RO into

Figure 6. The camera systems adopted for capturing image sequences during the landslide simulation experiments. In order: the pair of Nikon D200 high-resolution cameras; a single videocamera for surveillance; the pair of DALSA Falcon 4M60 high-speed cameras.

Downloaded by [Tiantian Feng] at 18:35 18 February 2014

the GRS. On the other hand, the scaling of the reconstruction could also be possible without GCPs, but only adopting one distance between two points that could be measured on the images, as described in Section 2.2.

A preliminary evaluation of the achievable precision of 3-D point coordinates can be worked out by using equations (1) and (2). The image coordinate precision will depend on the methods adopted for their measurement and then is expressed as a fraction k of the pixel size p. Moreover, precision will change according to the distance from the stereo-cameras and the slope surface (approximately from 2 m to 6 m). This would result in the range $\pm 0.36\ k$ mm to $\pm 1.08\ k$ mm in both directions parallel to the camera sensor planes, and in the range $\pm 0.51\ k$ mm to $\pm 4.63\ k$ mm in the orthogonal direction, i.e. along depth. Considering that k can always be assumed as lower than 1, the achievable precisions are compatible with the experiment requirements. Indeed, a precision on the 3-D coordinates of ± 10 mm of surface points was retained sufficiently for successive data analyses.

Downloaded by [Tiantian Feng] at 18:35 18 February 2014

4.2.1. Surface reconstruction. This technique is aimed at the generation of a digital surface model (DSM) for each observation epoch, i.e., from each pair of stereo-images. Camera set-up, calibration, and orientation procedures have already been described in the introduction of this subsection.

The photogrammetric procedure for DSM generation consists of the extraction of corresponding points from at least two images gathered at the same time, after calibration and image orientation. This task can be achieved in an automatic way by using *image matching* algorithms, which mainly exploits the similarity of image intensity between corresponding areas of different images. Moreover, the availability of a rough model of the surface and the relative orientation can help the matching process, as shown in figure 7. The former helps drive the matching process reducing the search space where one is looking for the homologous points. The latter can be used to establish a further constraint to check the results of matching, or even to be

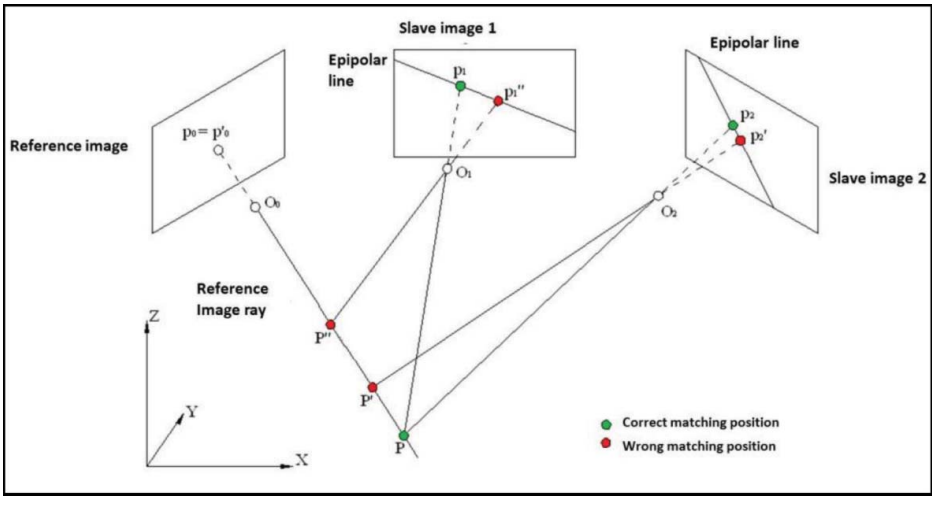

Figure 7. Example of the search of the homologous points of p_0 on the reference image on two other 'slaves' images (2 and 3).

integrated in the matching algorithm as in *multi-photo geometrically constrained matching* (MGCM) of Grün and Baltsavias (1988). In the case of a stereo-camera system, this geometric constraint is represented by the *epipolar line*: given a point on the first image (p_0) of the stereo-pair, the corresponding homologous point on the other image should lie on a line that can be worked out on the basis of the relative orientation parameters (see Hartley & Zissermann 2006). If three images are available, the constraint becomes even stronger because if the extracted homologous points are correct, they should closely intersect in a point in object space, as for the green point in figure 7. The accuracy of this intersection would depend on the precision of the location of matched points and on the quality of relative orientation. The denser the grid of computed points, the better will be the spatial resolution of the DSM. For this reason, in metrological applications of close-range photogrammetry the so-called *area-based dense matching* techniques are usually adopted for surface reconstruction. If more than two photos are available, a *multi-photo* approach can be applied to increase the reliability of the results whose quality can be internally checked thanks to the intersection of multiple rays (see figure 7).

Here the MGCM+ algorithm (Previtali et al. 2011) has been utilized for reconstructing the surface of the slope during the different steps of a landslide simulation experiment. This algorithm is an evolution of MGCM, which can exploit either the radiometric similarities of corresponding areas of two or more oriented images, and the geometric constraints given by the knowledge of the orientation between the images and the object. MGCM is based on the principle of *Least Squares matching* (LSM, Förstner 1982; Grün 1985): due to the different positions of the cameras, the content of each image will slightly differ from the others because of perspective deformations and radiometric changes. These variations can be locally compensated for by estimating some simple geometric and radiometric transformations that are valid in the neighbourhood of a point. Radiometric transformation can be replaced by local image equalization prior to matching or directly implemented into the functional model of LS. In the latter case, the use of additional radiometric parameters could lead to over-parameterization problems. Owing to this reason, here the local windows where matching is tried are equalized beforehand. In the MGCM+ algorithms some criteria for improving the selection of the best images to match in case of multiple overlaps have been included. On the other hand, here the availability of only two images does not fully allow exploiting the potential of such technique. Matching is based on radiometric similarities reinforced by the epipolar constraint, i.e., the homologous point should lie very close to epipolar line. Matching starts in the first image pair of the sequence, when the surface of the slope is still quite flat. A plane interpolating the average surface of the slope is enough to instantiate the matching process. Alternatively, some feature points extracted and matched with SIFT operator could be used as 'seed' points to interpolate a better initial surface. The process is applied in an iterative way as described in Previtali et al. (2011). The point cloud obtained at each step is adopted to interpolate a new initial surface as far as the required resolution of the DSM is reached.

Once DSMs at each epoch have been independently computed, these need to be compared to detect changes. This task requires a specific comment. A couple of DSMs cannot be compared in a pointwise manner because the points used to generate each DSM may differ. In addition, image matching can result in an irregular point cloud, having a different point density according to the local properties (roughness, texture, reflectivity, etc.) of each portion of the object. To overcome these

Downloaded by [Tiantian Feng] at 18:35 18 February 2014

Downloaded by [Tiantian Feng] at 18:35 18 February 2014

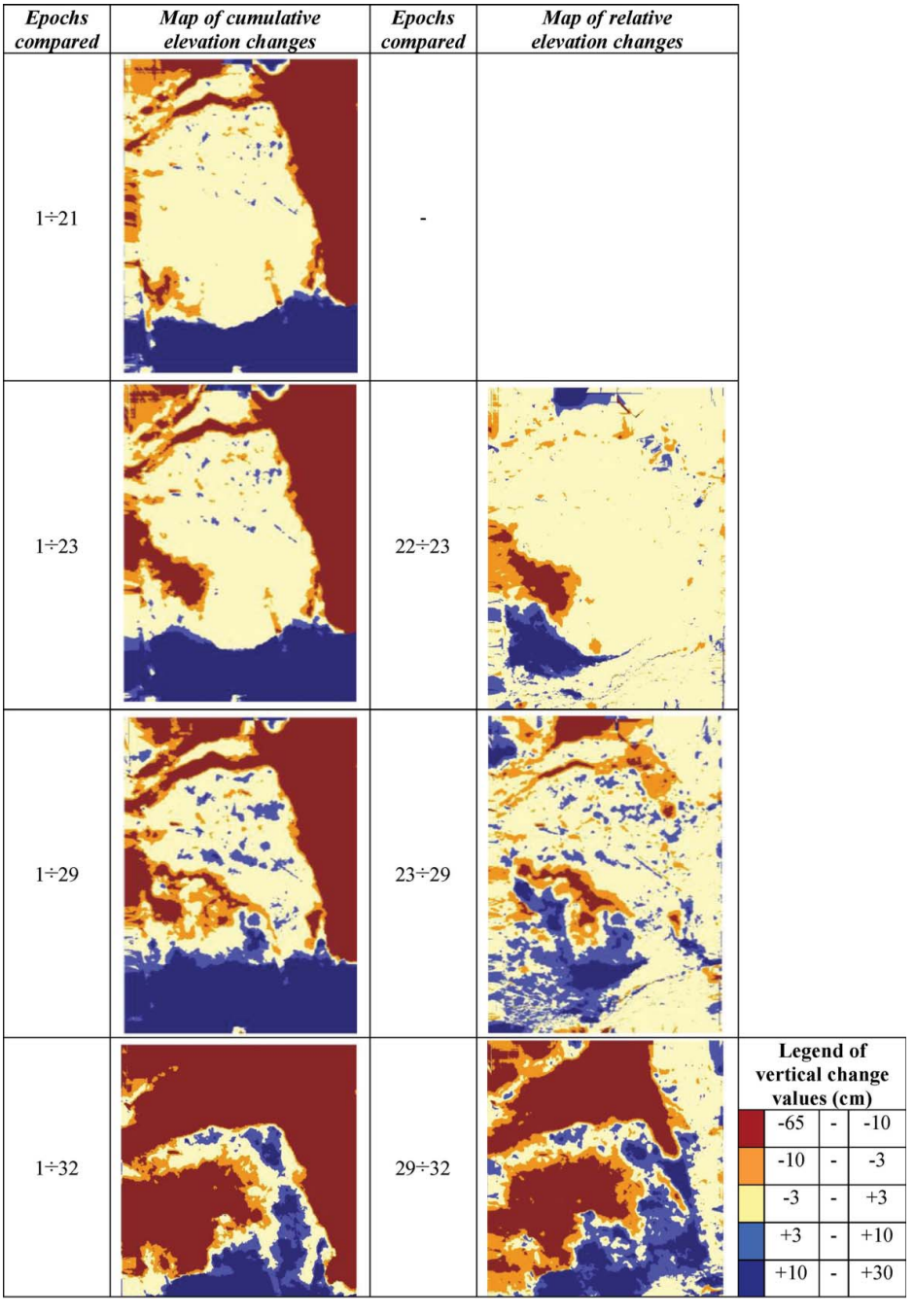

Figure 8. Maps of vertical changes during a landslide experiment; only the most representative epochs are illustrated here. Elevation changes have been referred to a plane interpolating the surface of the slope at the beginning of the experiment.

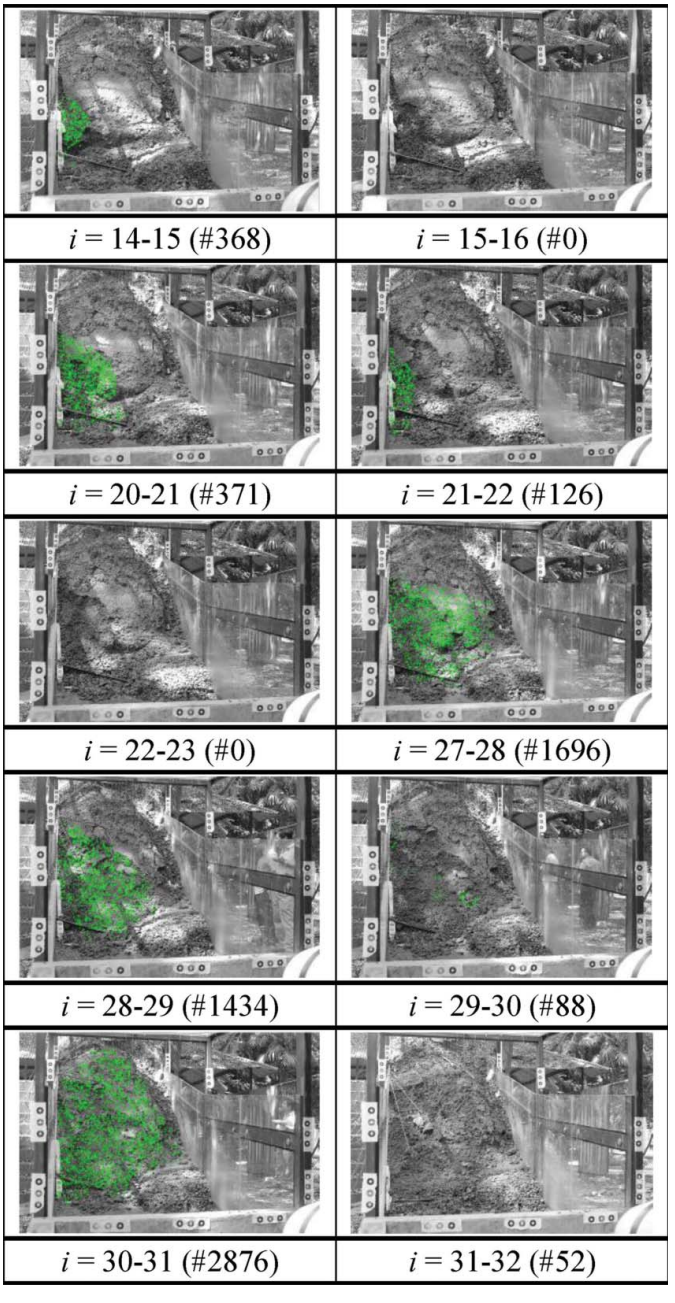

Figure 9. Displacements on the surface of the landslide model detected from *feature point tracking* (in green) from Feng et al. (2012).

problems, every DSM is interpolated along a regular grid whose coordinates are defined with respect to an assigned reference plane. The plane and the grid must be the same at both epochs. In the case under study, the average plane interpolating the reconstructed slope surface was selected as reference. A grid size of 5 × 5 mm was

Downloaded by [Tiantian Feng] at 18:35 18 February 2014

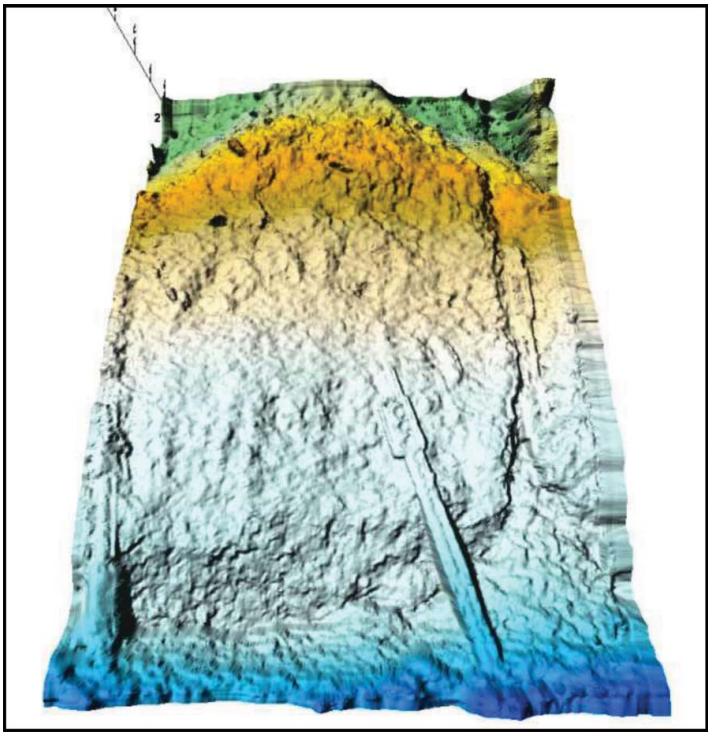

Figure 10. Image of the digital surface model produced with MGCM+ algorithm in correspondence of epoch 21.

adopted for interpolating points. The differences between the two surfaces were computed in correspondence with each grid node, yielding the maps reported in figure 8 where the elevation changes have been displayed. Here the chronicle of the experiment can be clearly seen. In the first period (from epoch 1÷21), a large erosion occurred on the right side of the slope, resulting in the accumulation of much debris at the toe. This process is visible in the corresponding image in figure 9. Also a pair of transversal fractures can be seen in the upper region. Then the main changes come up in the lower left area, up to the failure at epoch 32. These results were found to be coherent with another analysis based on the use of a *feature point tracking* (FPT) algorithm (see Feng et al. 2012) that was adopted to track a dense field of points on the slope surface during experiment (see figure 9).

A metric assessment of the solution was not possible because laser scanning was not available at the time of the experiment to provide benchmarking surfaces. On the other hand, the results obtained from the two methods (FPT and surface reconstruction) gave mutual validation, at least from a qualitative way. Moreover, the use of MGCM+ algorithm for surface reconstruction included an internal quality assessment, given by the use of geometric constraints in the LSM process. To show the quality of results, also a 3-D visualization of the surface reconstructed at epoch 21 is shown in figure 10.

An important remark is about the selection of the reference plane, which is really strategic because only volumetric changes along the normal direction to that can be

Downloaded by [Tiantian Feng] at 18:35 18 February 2014

evaluated. This involves that, in the case of more complex deformation processes, more reference planes have to be established.

5. Conclusions

In this paper some applications of photogrammetry to gather data during a landslide simulation experiment have been reported. Such examples would demonstrate how this non-contact technique may help scientists retrieve both qualitative and quantitative information during a wide range of laboratory tests for hydrogeological risk assessment.

The application of photogrammetry today is simpler than in the past thanks to the development of digital techniques and automation of the processes such as camera calibration, image orientation, and surface reconstruction. The availability of 3-D imaging sensors, also at low cost, can be exploited to enrich and improve the information that can be obtained from purely image-based methods. For example, in case some features should be extracted or tracked along time (like in the example reported in Section 3.2), images are more convenient.

In the case of surface reconstruction, the use of ranging devices might be simpler. Also in this case, however, the use of the state-of-the-art image-based techniques has been proven to give out very detailed digital surface models, comparable to the ones that can be produced by using 3-D scanning sensors, but at a much cheaper cost (see Section 4.2).

On the other hand, the impressive technological development does not replace the role of users, who must be aware of photogrammetric techniques and should use them in a rigorous manner. This consideration also entails data interpretation. Photogrammetry provides mainly area-based information the understanding of which might be more different than in the case of traditional point-based measurements.

Downloaded by [Tiantian Feng] at 18:35 18 February 2014

Funding

This study is supported by the 863 National High Technology Research and Development Program of China [grant number 2012AA121302]; the 973 Basic National Research Program of China [grant number 2013CB733204]; the National Science Foundation of China [grant number 41171327], [grant number 41201379]; the Specialized Research Fund for the Doctoral Program of Higher Education [grant number 20120072120057]. This research partially benefited from the support of the FIRB 2010 National Research Program of the Italian Ministry of University and Research (MIUR).

Note

This research was partially presented at the International Workshop 'The Role of Geomatics in Hydrogeological Risk', Padua (Italy), 27–28 February 2013.

References

Barazzetti L. 2011. Planar metric rectification via parallelograms. In: Remondino F, Shortis MR, editors. Proc. SPIE 8085, Videometrics, Range Imaging, and Applications XI; 2011 May 23–26; Munich (Germany).

Barazzetti L, Scaioni M. 2009. Crack measurement: development, testing and applications of an automatic image-based algorithm. ISPRS J Photogramm Remote Sens. 64:285–296.

Barazzetti L, Scaioni M. 2010. Development and implementation of image-based algorithms for measurement of deformations in material testing. Sensors. 10:7469–7495.

Brasington J, Smart RMA. 2003. Close range digital photogrammetric analysis of experimental drainage basin evolution. Earth Surf Processes Landforms. 28:231–247.

Budzier H, Garlach G. 2011. Thermal infrared sensors, theory, optimization and practice. Chichester: John Wiley & Sons.

Chandler JH, Buffin-Belanger T, Rice S, Reid I, Graham DJ. 2003. The accuracy of a river bed moulding/casting system and the effectiveness of a low-cost digital camera for recording river bed fabric. Photogramm Rec. 18:209–223.

Chandler JH, Fryer JG, Jack A. 2005. Metric capabilities of low-cost digital cameras for close range surface measurement. Photogramm Rec. 20:12–26.

Feng T, Liu X, Scaioni M, Lin X, Li R. 2012. Real-time landslide monitoring using close-range stereo image sequences analysis. Paper presented at: Systems and Informatics. 2012 International Conference; Yantai, China.

Förstner W. 1982. On the geometric precision of digital correlation. Int Arch Photogramm. 24(3):176–189.

Fraser CS. 1992. Photogrammetric measurement to one part in a million. Photogramm Eng Remote Sens. 58:305–309.

Fraser CS. 1996. Network design. In: Atkinson KB, editor. Close range photogrammetry and machine vision. Dunbeath, Scotland: Whittles Publishing; p. 256–281.

Fraser CS. 2013. Automatic camera calibration in close range photogrammetry. Photogramm Eng Remote Sens. 79:381–388.

Fukuzono T. 1990. Recent studies on time prediction of slope failure. Landslide News. 4:9–12.

Gessese GD, Fuchs H, Mansberger R, Klik A, Rieke-Zapp DH. 2010. Assessment of erosion, deposition and rill development on irregular soil surfaces using close range digital photogrammetry. Photogramm Rec. 25:299–318.

Gigli G, Fanti R, Canuti P, Casagli N. 2011. Integration of advanced monitoring and numerical techniques for the complete risk scenario analysis of rockslides: the case of Mt. Beni (Florence, Italy). Eng Geol. 120:48–59.

Grün A. 1985. Adaptive least squares correlation: a powerful image matching technique. S Afr J Photogramm Remote Sens Cartogr. 14:175–187.

Grün A. 2012. Development and status of image matching in photogrammetry. Photogramm Rec. 27:36–57.

Grün A, Baltsavias EP. 1988. Geometrically constrained multiphoto matching. Photogramm Eng Remote Sens. 54:633–641.

Guidi G, Russo M, Beraldin JA. 2010. Acquisizione 3-D e modellazione poligonale. Milano: McGraw-Hill.

Hartley R, Zissermann A. 2006. Multiple view geometry in computer vision. Cambridge: Cambridge University Press.

Heng BCP, Chandler JH, Armstrong A. 2010. Applying close range digital photogrammetry in soil erosion studies. Photogramm Rec. 25:240–265.

Kabdasli MS, Celikoyan TM, Seker DZ, Aydingakko A. 2004. Application of digital photogrammetry and image processing techniques for hydraulic model experiments. Int Arch Photogramm Remote Sens Spat Inf Sci. 35(B/3):739–743.

Kraus K. 2008. Photogrammetry - Geometry from images and laser scans. Berlin: Walter de Gruyter.

Löwe DG. 2004. Distinctive image features from scale-invariant keypoints. Int J Comput Vision. 60:91–110.

Luhmann T, Robson S, Kyle S, Boehm J. 2013. Close range photogrammetry: 3D imaging techniques. Berlin: Walter De Gruyter Inc.; p. 702.

Maas HG, Hampel U. 2006. Photogrammetric techniques in civil engineering material testing and structure monitoring. Photogramm Eng Remote Sens. 72:39–45.

Downloaded by [Tiantian Feng] at 18:35 18 February 2014

Pirotti F, Guarnieri A, Vettore A. 2013a. State of the art of ground and aerial laser scanning technologies for high-resolution topography of the earth surface. Eur J Remote Sens. 46:66–78.

Pirotti F, Guarnieri A, Vettore A. 2013b. Ground filtering and vegetation mapping using multi-return terrestrial laser scanning. ISPRS J Photogramm Remote Sens. 76:56–63.

Pozzoli A, Mussio L, Scaioni M. 2004. A project for the survey of a hydraulic stream confluence model based on a general procedure for three-image orientation. Paper presented at: Commemorative Volume for the 60th birthday of Prof. Dr. Armin Grün. Zurich.

Previtali M, Barazzetti L, Scaioni M, Tian Y. 2011. An automatic multi-image procedure for accurate 3-D object reconstruction. Paper presented at: 4th International Congress on Image and Signal Processing. Shanghai, P.R. China.

Qiao G, Lu P, Scaioni M, Xu S, Tong X, Feng T, Wu H, Chen W, Tian Y, Wang W, Li R. 2013. Landslide investigation with remote sensing and sensor network: from susceptibility mapping and scaled-down simulation towards in situ sensor network design. Remote Sens. 5:4319–4346.

Remondino F, Stoppa D. 2013. TOF range-imaging cameras. Berlin: Springer-Verlag.

Rieke-Zapp DH, Nearing MA. 2005. Digital close range photogrammetry for measurement of soil erosion. Photogramm Rec. 20:69–87.

Roncella R, Romeo E, Barazzetti L, Gianinetto M, Scaioni M. 2012. Comparative analysis of digital image correlation techniques for in-plane displacement measurements. Paper presented at: 5th International Congress on Image and Signal Processing (CISP12). Chongqing, P.R. China.

Roncella R, Scaioni M, Forlani G. 2004. Application of digital photogrammetry in geotechnics. Int Arch Photogramm Remote Sens Spat Inf Sci. 35(B/3):93–98.

Rossi MJ, Ares JO. 2012. Close range stereophotogrammetry and video imagery analyses in soil ecohydrology modeling. Photogramm Rec. 27:111–126.

Scaioni M, Lu P, Feng T, Chen W, Wu H, Tong X, Wang W, Li R. 2013. Analysis of spatial sensor network observations during landslide simulation experiments. Eur J Environ Civ Eng. 17:802–825.

Tiwari V, Sutton MA, McNeill SR. 2007. Assessment of high speed imaging systems for 2D and 3D deformation measurements: methodology development and validation. Exp Mech. 4:561–579.

Vosselman G, Maas HG. 2010. Airborne and terrestrial laser scanning. Boca Raton: Taylor and Francis.

Watanabe K, Koseki J, Tateyama M. 2005. Application of high-speed digital CCD cameras to observe static and dynamic deformation characteristics of sand. ASTM Geotech Test J. 5:423–435.

Downloaded by [Tiantian Feng] at 18:35 18 February 2014